

Unraveling the dust activity of naked-eye comet C/2022 E3 (ZTF)

Bin Liu^{1,2} and Xiaodong Liu^{1,2}

¹ School of Aeronautics and Astronautics, Shenzhen Campus of Sun Yat-sen University, Shenzhen, Guangdong 518107, China

² Shenzhen Key Laboratory of Intelligent Microsatellite Constellation, Shenzhen Campus of Sun Yat-sen University, Shenzhen, Guangdong 518107, China
e-mail: liuxd36@mail.sysu.edu.cn

ABSTRACT

A morphological and photometric analysis of the naked-eye long-period comet C/2022 E3 (ZTF) before perihelion is presented in this study. The observation images taken by the Zwicky Transient Facility survey telescope from July 2022 to October 2022 show a gradually brightening dust coma and a tail with a clear structure. The morphology of the dust coma reveals nonsteady-state emission with an ejection velocity lower than 14 m s^{-1} for particles larger than $100 \mu\text{m}$. According to the syndyne-synchrone analysis, dust particles larger than about $10 \mu\text{m}$ contribute significantly to the observed tail. The model simulations of the 10 October 2022 image suggest that the radii of large particles lingering near the nucleus range from 0.1 mm to 1 mm . Assuming that the nucleus of comet E3 is a homogeneous sphere with an albedo of 0.1 , the photometry analysis sets the lower and upper limits of the nucleus radius to be $0.81 \pm 0.07 \text{ km}$ and $2.79 \pm 0.01 \text{ km}$, respectively. The dust production rates increased continuously from $241 \pm 3 \text{ kg s}^{-1}$ in July to $476 \pm 9 \text{ kg s}^{-1}$ in October. The dependence of the ejection velocity v_{\perp} perpendicular to the orbital plane of comet E3 on the particle size a can be simplified as $v_{\perp} \propto a^{-1/2}$, which indicates that the dust emission is likely driven by gas. The water-production rate is inferred as $\sim 368 \pm 72 \text{ kg s}^{-1}$ in October 2022, which is sustained by an equilibrium-sublimating area of $8.2 \times 10^6 \text{ m}^2$ at least. The comparative analysis of the characteristics of comet E3 with those of comets belonging to different types shows that the activity profile of long-period comet E3 surprisingly aligns more closely with those of short-period comets within a heliocentric distance range of about $[1.7, 3.4] \text{ AU}$, where the images of comet E3 that we used in this study were taken.

Key words. comets: general / comets: individual: 2022 E3 (ZTF) / methods: observational / methods: numerical / techniques: photometric

1. Introduction

Long-period comets (LPCs) are classified from a dynamical perspective as comets with orbital periods exceeding 200 years. They are characterized by random orbital inclinations and typically exhibit high eccentricities (Lowry et al. 2008). According to the dynamical evolution model of the early Solar System, LPCs originally formed in the giant planet region (the heliocentric distance ranging from 5 AU to 30 AU) about 4.6 billion years ago (Lippi et al. 2023). Subsequently, due to the influence of the orbital migration of giant planets, LPCs were ejected into the outer reaches of the Solar System before they eventually reached their reservoir, known as the Oort cloud, which consists of 10^{12} to 10^{13} comets with semimajor axes ranging from $10^{3.5} \text{ AU}$ to 10^5 AU (Wiegert & Tremaine 1999; Nesvorný 2018). Unlike short-period comets (SPCs), LPCs have experienced minimum heating and sublimation processes since their formation. Their nuclei remain frozen for the majority of their lifetime, suggesting that the material within the nuclei of LPCs has undergone limited alteration since their formation and has largely retained its initial composition (Opitom et al. 2015). Hence, the study of LPCs provides a deep understanding of the compositions and conditions of comets at the time of their formation, as well as of the evolution of the protoplanetary disk (Hands & Dehnen 2020).

LPCs whose orbital paths partially lie within the inner regions of the Solar System undergo continuous heating from solar radiation as they approach perihelion. This process typically leads to the sublimation of volatiles within the nucleus, resulting in the dust activities on the surface of the nucleus (Garcia

& Gil-Hutton 2021). With the increasing activity of the nucleus, the comet displays the appearance of either a coma or a dust tail (Kareta 2021). The dust particles in the coma and tail originate from the nucleus, the analysis of which can provide insights into the activity mechanisms and physical properties of LPCs (Mumma & Charnley 2011). However, conducting in situ measurements of LPCs is challenging because the LPC activities are unpredictable (Forbes & Loeb 2019), and the current commonly used method for studying the dust activities of LPCs is through observations of specific target areas.

The long-period comet C/2022 E3 (ZTF), hereafter "E3", was discovered on 2 March 2022 with the 48-inch Schmidt-type telescope of the Zwicky Transient Facility (ZTF), with an apparent magnitude of approximately 17.3 at a heliocentric distance of about $R = 4.3 \text{ AU}$ (Bolin et al. 2022). The orbit of comet E3 meets the characteristics of Oort-cloud comets, with an eccentricity of 1.0007, an osculating semimajor axis of -4087 AU , and an inclination of 109° . Comet E3 reached its perihelion on 12 January 2023 with a heliocentric distance of 1.11 AU . Comet E3 made its closest approach to Earth on 31 January 2023. This observation geometry caused comet E3 to appear quite bright and visible to the naked eye from the Earth, with an apparent magnitude of 5². This provides a good opportunity for a detailed characterization of the physical properties of comet E3, which is a long-period comet. The closest distance between comet E3 and Earth is only 0.28 AU , indicating that comet E3 is a near-Earth

¹ https://ssd.jpl.nasa.gov/tools/sbdb_query.html

² <http://www.cobs.si/>

object. Because the warning time during the first approach of E3 to Earth was limited, it is essential to pay special attention to this comet.

Comet E3 showed cometary features when it was discovered in March 2022 (Bolin et al. 2022), including a green coma, a thin ion tail, and a dispersed yellowish dust tail. As the heliocentric distance of comet E3 decreases with time after its discovery, the solar heat accelerates sublimation of the volatiles on the surface of the nucleus, which produces more gases and increases the brightness of the green coma of comet E3. The appearance of the green coma of comet E3 is probably due to the diatomic carbon (C_2) in the resulting gases by sublimation (Borsovsky et al. 2021; Bolin et al. 2024; Mugrauer 2023). The thin ion tail pointed to the antisolar direction, and the yellowish dust tail lay between the antisolar direction and the antivelocitv direction of comet E3 (Bolin et al. 2022). Additionally, an antitail pointing to the Sun became visible when the Earth was close to the orbital plane of comet E3³. Shortly after passing through its perihelion, comet E3 encountered a coronal mass ejection, the resulting solar wind from which broke up its ion tail⁴. Comet E3 has now moved beyond 4 AU away from the Sun.

The rotation period of the nucleus of E3 was determined to be about 8.49 hours from an analysis of the morphology of the coma in images from the Savonarola Cassegrain telescope, as reported by Manzini et al. (2023). For comparison, Knight et al. (2023) reported an apparent period of 8.7 hours using the Lowell Observatory Hall telescope and the Lowell Discovery telescope. Amateur photometric data showed that the brightness of comet E3 continuously increased throughout 2022. The OH production rate was approximately $Q_{OH} = 1.54 \times 10^{28} \text{ s}^{-1}$ on 17 October 2022, as obtained from the TRAPPIST robotic telescopes (Jehin et al. 2011), and it increased to $Q_{OH} = 3.51 \times 10^{28} \text{ s}^{-1}$ in the observation taken on 19 December 2022, as the distance from the Sun decreased from 1.96 AU to 1.18 AU (Jehin et al. 2022a,b). The sequence of post-perihelion observation data taken by the Trivandrum Observatory in February 2023 showed a noticeable decrease in the apparent sizes of the head and tail of comet E3 (Jayakrishnan et al. 2023). The CN, C_3 , and C_2 production rates on 10 March 2023 were approximately $(5.43 \pm 0.11) \times 10^{25} \text{ mol/s}$, $(2.01 \pm 0.04) \times 10^{24} \text{ mol/s}$, and $(3.08 \pm 0.5) \times 10^{25} \text{ mol/s}$, respectively (Bolin et al. 2024).

The European Space Agency (ESA) plans to launch a fast-class (F-class) exploration mission in 2028, named *Comet Interceptor* (CI) (Snodgrass & Jones 2019). CI aims to explore an unknown target, which is classified as a dynamically new comet (a subset of LPCs) (Jones & Snodgrass 2019; Snodgrass & Jones 2019). The CI spacecraft will initially travel toward the Sun-Earth L_2 Lagrangian point and remain there until a suitable target is identified (Schwamb et al. 2020). The CI spacecraft are planned to be equipped with a dust analyzer, which will collect dust grains from the coma and tail of the comet (Moore et al. 2021). Based on the physical properties of LPCs, it is expected that the currently unknown target comet is likely to be in a highly active state. Thus, in preparation for the mission, it is necessary to investigate the dust activity of celestial bodies such as LPCs. Although comet E3 is moving away from the inner Solar System, it is considered to be "the most promising virtual target for CI" (Kueppers 2023). Hence, the analysis of the dust activity of comet E3 is important for the science and mission planning of CI.

In this study, we present a morphological and photometric analysis of comet E3 in the images recorded in public science archives to enhance the understanding of its pre-perihelion activity. The structure of the paper is as follows. Section 2 describes the comet E3 archive that is used in the work in detail. Section 3 presents the results of the morphological and photometric analysis. The dust properties, nucleus size, production rates, and sublimating area are discussed in Section 4. Section 5 summarizes the conclusions of this study.

2. Data

The publicly available archival data (IRSA 2020) of comet E3 that are analyzed in this paper are from the ZTF (Bellm et al. 2018), which is mounted on the 48-inch Schmidt-type telescope of the Palomar Observatory. The ZTF is equipped with a 600 megapixel cryogenic charge-coupled device camera, which provides an image scale of $1''$ per pixel and a field of view of about 47 square degrees. All ZTF images of comet E3 have exposure times of 30 s and are made in the r band. The images of comet E3 were taken from July 2022 to October 2022. It should be noted that only the images taken pre-perihelion were used for analysis in this paper because no images taken post-perihelion that showed clear dust coma and tail are available. For ZTF images taken on different dates, we removed rays across the entire range of the original image (Joye & Mandel 2003). By interpolating the areas of the image that were affected by rays with the average pixel count of the surrounding regions, we obtained a cleared image that is free from the effects of the rays (Bertin & Arnouts 1996). The process of data reduction was completed with the Astroart software (Nicolini et al. 2003). The details of the observing geometries are listed in Table 1.

3. Results

3.1. Morphology

The images of comet E3 at five different observation epochs are shown in Figure 1. The coma exhibited a relative symmetrical appearance, and its brightness increased with time. The extended appearance is visible in all observed images. The direction of the tail at different epochs generally lies between the projected direction from the Sun to comet E3 and the antivelocitv direction of the projected motion of comet E3, which is a distinctive feature of the dust tails. The length of the tail of comet E3 in the image taken on 13 July 2022 was about $80''$ (126000 km), and in the image taken on 10 October 2022, it extended to about $150''$ (245000 km).

The surface brightness profiles were determined within a series of concentric annular apertures measured from the optocenter of the coma. Each single annular aperture has a width of $1''$, extending to a radius of $30''$. The sky background was determined in an annulus aperture with an inner radius of $80''$ and an outer radius of $120''$. The brightness profiles and their uncertainties resulting from background subtraction for the first and last observed images (13 July and 10 October 2022) are shown in Figure 2. The distribution of the surface brightness $\Sigma(\theta)$ is well fit to a power-law relation of $\Sigma(\theta) \propto \theta^q$, with $q = -1.61 \pm 0.02$ on 13 July 2022 and $q = -1.94 \pm 0.03$ on 10 October 2022, where θ is the angular distance measured from the nucleus in arcseconds. The index q can describe the dynamical state of the coma. For a steady-state coma, the range of the index q is between -1 and -1.5, where the limiting cases of $q = -1$ and $q = -1.5$ correspond to the cases of the absence and the dominance of the so-

³ <http://www.spaceweather.com/> (Archive, 22 January 2023)

⁴ <http://www.spaceweather.com/> (Archive, 19 January 2023)

Table 1: Observation geometries of comet E3

Date (UT)	DOY ^a (days)	R^b (AU)	Δ^c (AU)	α^d (deg)	PsAng ^e (deg)	PsAMV ^f (deg)	ν^g (deg)	δ^h (deg)
13 Jul 2022	193	2.86	2.18	17.6	163.9	150.4	257.2	-5.5
26 Jul 2022	202	2.70	2.12	19.9	141.3	141.5	259.7	-0.1
06 Aug 2022	217	2.58	2.11	22.2	125.0	134.4	262.0	4.6
06 Sep 2022	248	2.22	2.20	26.3	90.5	119.7	269.9	16.1
10 Oct 2022	282	1.83	2.25	25.8	57.8	110.8	282.1	23.5

^a Day of year, 2022/01/01 = 1.

^b Distance between comet E3 and the Sun.

^c Distance between comet E3 and the Earth.

^d Phase angle, Sun-E3-Earth.

^e Angle between the Sun-E3 direction and the north direction (measured counterclockwise).

^f Angle between the negative projected heliocentric velocity vector and the north direction (measured counterclockwise).

^g True anomaly of comet E3.

^h Angle of the observer from the orbital plane of comet E3.

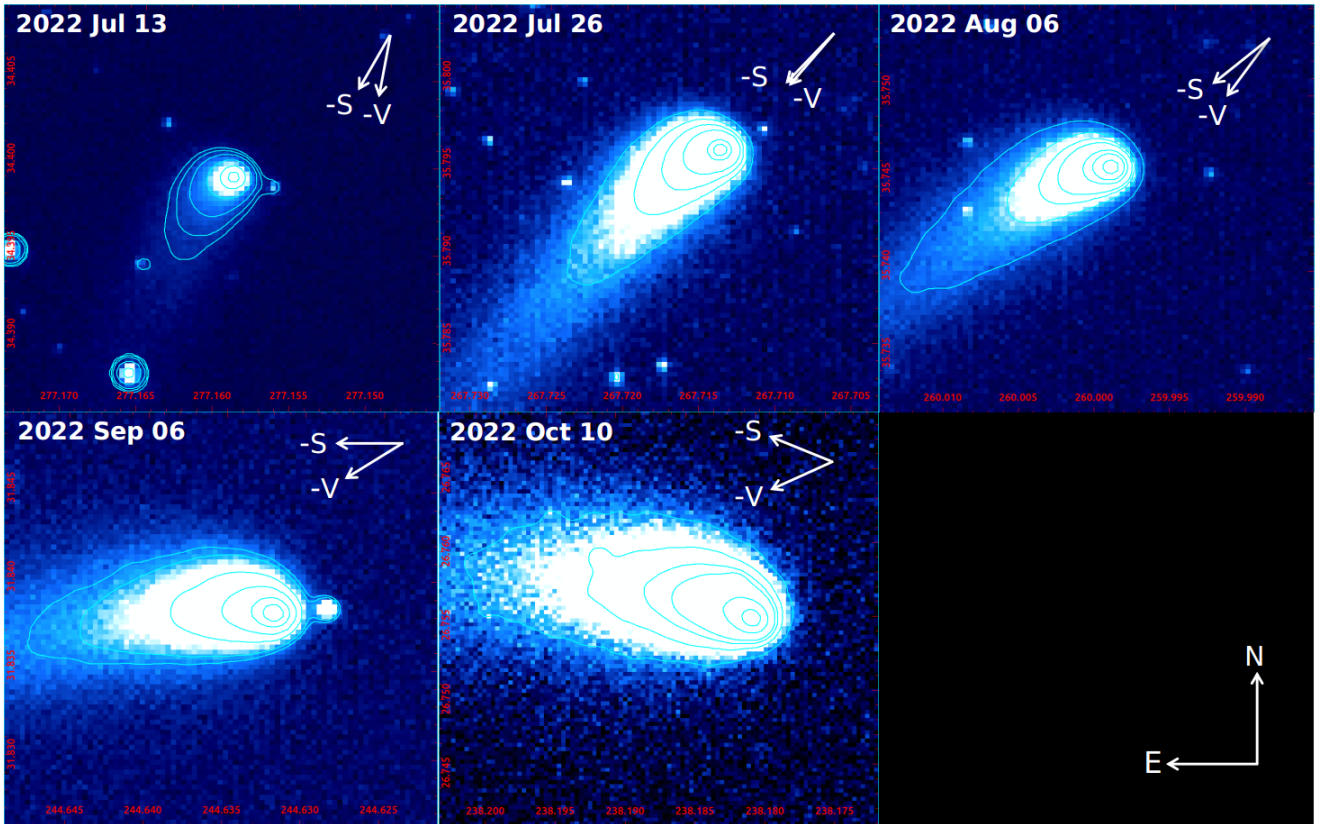


Fig. 1: Composite images of comet E3. The observation epoch is marked in the upper left corner of each panel. The projected Sun-E3 radial direction (-S) and the antivelocidity direction of the projected motion of comet E3 (-V) are indicated as white arrows. The values of the right ascension and declination are shown in each panel (red text).

lar radiation pressure, respectively (Jewitt & Meech 1987). The obtained indices for comet E3 strongly deviate from the typical value of a steady-state coma, which may suggest changes in the dust (Farnham 2009). These deviations are likely caused by the existence of the nonsteady-state emission. The surface brightness profiles were also determined for the images taken on 26 July 2022, 6 August 2022, and 6 September 2022, with indices of -1.65 ± 0.02 , -1.74 ± 0.03 , and -1.81 ± 0.03 , respectively. As the heliocentric distance of comet E3 (Table 1) decreased, the

index q increased, suggesting a potential correlation between the heliocentric distance and the index. The research of this correlation relies on the detailed modeling of the dust coma, which is beyond the scope of the present study.

Following Equation (4) from Jewitt & Meech (1987), the ejection speed of particles v_{ej} can be estimated by

$$v_{ej} = \frac{\sqrt{2\beta\mu_{\odot}\Delta \tan l_{coma} \sin \alpha}}{R}, \quad (1)$$

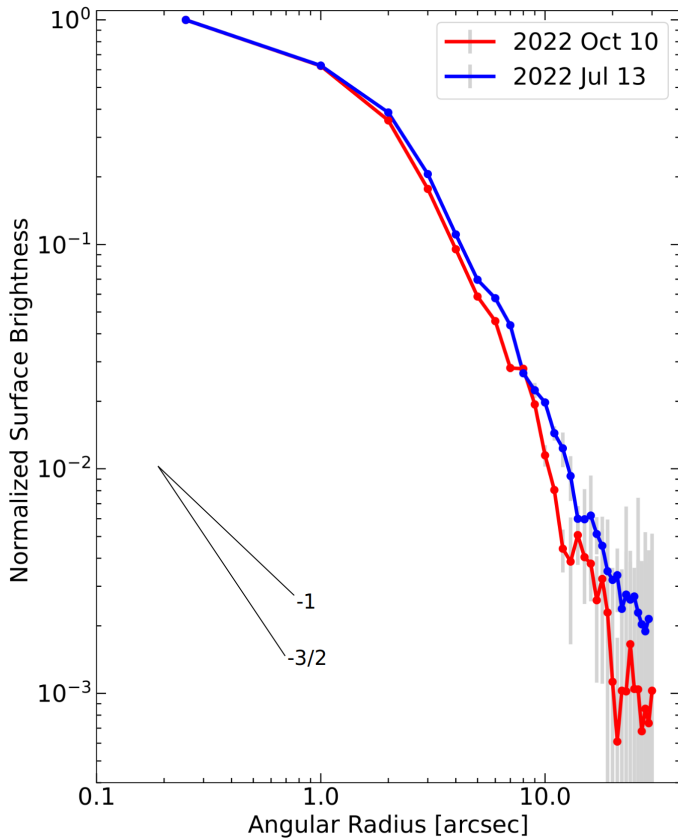


Fig. 2: Brightness profiles of the coma measured on 13 July (blue line) and 10 October (red line) 2022. The black lines show the logarithmic gradients of $q = -3/2$ and $q = -1$.

where $l_{\text{coma}} \sim 10''$ (1.5×10^7 m) is the length of the dust coma extending toward the Sun, $\mu_{\odot} = 3.96 \times 10^{-14}$ AU³ s⁻² represents the gravitational constant of the Sun, and $\beta = C_{\text{pr}} Q_{\text{pr}} / (2\rho a)$ is a dimensionless factor that represents the ratio of the solar radiation pressure relative to the solar gravity acting on the dust particles (Burns et al. 1979; Moreno et al. 2017). Here, a is the particle radius, ρ is the particle bulk density, which is assumed to be $\rho = 500$ kg/m³ (Groussin et al. 2019), and C_{pr} and Q_{pr} are the solar radiation pressure parameters, the values of which were adopted as 1.19×10^{-3} m s⁻² and 1, respectively (Burns et al. 1979; Moreno et al. 2017). Substituting R , Δ , and α of different epochs (Table 1) in Equation 1, we estimated the ejection speed as $v_{\text{ej}} \sim 139\beta^{1/2}$ m s⁻¹. For instance, the value of ejection speed is approximately 14 m s⁻¹ for particles with a radius of 100 μm .

3.2. Photometry

A quantitative analysis is presented for the data of comet E3 at five different observation epochs, using five different sizes of circular photometry apertures with projected radii ranging from 1000 km to 160000 km. The sky background and its uncertainty were also measured in an annulus aperture with an inner radius of 80'' and an outer radius of 120'' as in Section 3.1. To obtain the absolute magnitudes H in r band, the apparent magnitudes $m_r(R, \Delta, \alpha)$ were reduced to the magnitude at a phase angle of zero degrees and the heliocentric and geocentric distances of one AU by equation

$$H = m_r(R, \Delta, \alpha) - 5 \log_{10}(R\Delta) - f(\alpha), \quad (2)$$

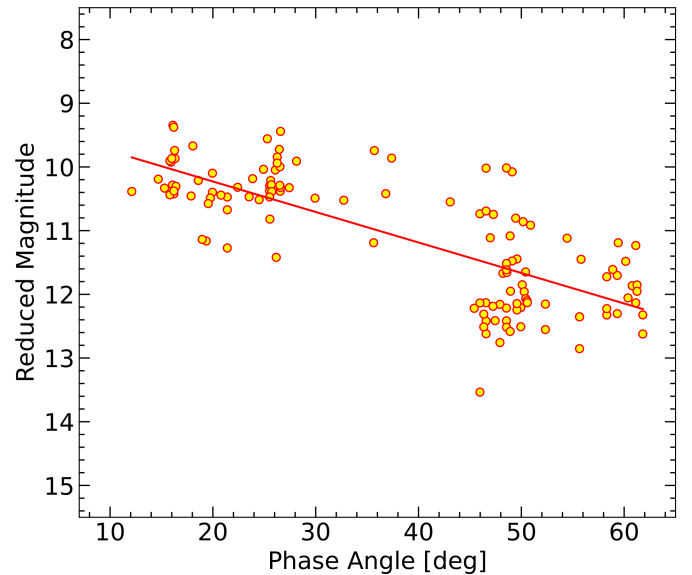


Fig. 3: Reduced magnitude vs. phase angle of comet E3 from 22 March 2022 to 26 March 2023. The filled yellow circles denote the observation data obtained from *CometasObs*. The red line represents the fitting of the data with a slope of (0.048 ± 0.003) mag deg⁻¹.

where R and Δ are defined in Table 1. The phase function $f(\alpha)$ can be assumed as a linear function $f(\alpha) = \gamma\alpha$ (Delahodde et al. 2001). Because only a limited sample size is available in the ZTF dataset, the linear coefficient γ was derived from the amateur photometric data observed by *CometasObs*⁵ covering the period from 22 March 2022 to 26 March 2023. The magnitude m was reduced to the magnitude at the geocentric and heliocentric distances of one AU (Moreno et al. 2012), and the relation between the reduced magnitudes m and the phase angle α is shown in Figure 3. Figure 3 shows that the brightness roughly increases as the phase angle decreases, although the brightness may not solely depend on the phase angle because variations in the activity of E3 at different phase angles might also be a contributing factor. The value of the linear coefficient γ , (0.048 ± 0.003) mag deg⁻¹ was obtained by fitting the data in Figure 3, and the phase function $f(\alpha)$ can be simplified and expressed as 0.048α .

From Jewitt et al. (2019a), the effective scattering cross section, C_e [km²], was derived from the resulting absolute magnitude,

$$C_e = \frac{1.5 \times 10^6}{p} 10^{-0.4H}, \quad (3)$$

where p is the geometric albedo. For cometary dust, it is appropriate to assume $p = 0.1$ (Ivanova et al. 2023). The values of the resulting apparent magnitudes, the absolute magnitudes, and the effective scattering cross section and their uncertainties for all epochs of observations are listed in Table 2. The uncertainty in Table 2 includes only the errors from photometric measurements and does not account for the errors introduced by the determination of the phase function.

⁵ <http://www.astrosurf.com/Cometas-Obs>

Table 2: Photometry result within apertures of fixed radii

Date	Property ^a	1000 km	2000 km	4000 km	8000 km	16000 km
13 Jul 2022	<i>V</i>	17.25 ± 0.03	15.94 ± 0.02	14.86 ± 0.03	14.21 ± 0.05	13.73 ± 0.06
13 Jul 2022	<i>H</i>	12.47 ± 0.03	11.15 ± 0.02	9.98 ± 0.03	9.38 ± 0.05	8.91 ± 0.06
13 Jul 2022	<i>C_e</i>	153.49 ± 3.49	515.34 ± 4.74	1399.88 ± 86.37	2547.37 ± 11.7	3945.41 ± 72.02
26 Jul 2022	<i>V</i>	17.11 ± 0.02	15.88 ± 0.02	14.71 ± 0.04	14.11 ± 0.03	13.66 ± 0.04
26 Jul 2022	<i>H</i>	12.37 ± 0.02	11.15 ± 0.02	9.98 ± 0.04	9.38 ± 0.03	8.91 ± 0.04
26 Jul 2022	<i>C_e</i>	168.33 ± 2.34	518.78 ± 8.17	1520.89 ± 48.27	2666.21 ± 83.41	4109.26 ± 163.86
06 Aug 2022	<i>V</i>	17.07 ± 0.04	15.84 ± 0.03	14.61 ± 0.02	13.96 ± 0.04	13.48 ± 0.03
06 Aug 2022	<i>H</i>	12.35 ± 0.04	11.13 ± 0.03	9.89 ± 0.02	9.25 ± 0.04	8.78 ± 0.03
06 Aug 2022	<i>C_e</i>	171.09 ± 5.09	528.51 ± 13.17	1666.27 ± 36.37	3002.61 ± 117.36	4614.93 ± 125.59
06 Sep 2022	<i>V</i>	16.32 ± 0.03	15.29 ± 0.02	14.41 ± 0.03	13.62 ± 0.04	13.11 ± 0.03
06 Sep 2022	<i>H</i>	11.66 ± 0.03	10.63 ± 0.02	9.75 ± 0.03	8.96 ± 0.04	8.44 ± 0.03
06 Sep 2022	<i>C_e</i>	328.16 ± 11.87	839.64 ± 15.09	1888.39 ± 51.08	3945.41 ± 177.17	6253.04 ± 114.09
10 Oct 2022	<i>V</i>	15.61 ± 0.05	14.98 ± 0.03	13.79 ± 0.02	13.07 ± 0.03	12.48 ± 0.02
10 Oct 2022	<i>H</i>	11.33 ± 0.05	10.71 ± 0.03	9.53 ± 0.02	8.81 ± 0.03	8.21 ± 0.02
10 Oct 2022	<i>C_e</i>	442.37 ± 21.18	787.21 ± 28.26	2315.99 ± 44.66	4526.61 ± 159.92	7812.26 ± 154.43

^a *V*: apparent magnitude, *H*: absolute magnitude, *C_e*: effective scattering cross section in km².

4. Discussion

4.1. Dust properties

It is possible to determine the physical properties of the cometary grains from the morphology of the coma and tails (Kim et al. 2022). The syndyne-synchrone method based on the Finson-Probstein theory (Finson & Probstein 1968) was employed to analyze the morphology of comet E3. The syndyne-synchrone method assumes that only solar gravity and the solar radiation pressure force act on the dust particles. A syndyne corresponds to the loci of the particles that are released continuously with a constant β . A synchrone line corresponds to loci of the particles that are released at the same time with various β . For the purpose of model simplification, the ejection speed of the particles was not taken into account when we used the syndyne-synchrone method. During all observation dates, the appearances of comet E3 were clear. Thus, it is appropriate to analyze the morphology of comet observed on five different dates using the syndyne-synchrone method with five dense syndyne-synchrone grids. The syndynes were plotted from $\beta = 0.0001$ to $\beta = 1$ with a step of an order of magnitude, and the synchrones are plotted from two years before the observation date up to the observation date with an interval of one day. In Figure 4, sparser syndyne-synchrone grids than what we used for the fitting are overplotted on the images for better visualization. Consistent fitting results that can explain all observations were obtained through analyzing the morphology of comet E3 in all images using the syndyne-synchrone grids. The linear jet-like feature is well fit by the synchrone representing about 10 August 2022, and dust particles larger than about 10 μm contribute significantly to the observed tail. The syndyne-synchrone method may no longer be reliable when the upper limit of the grain size is estimated. This is because large particles may linger around the nucleus, which usually cannot be resolved, and they are optically unimportant.

In order to estimate the upper limit of the grain size, we simulated the modeling of the 10 October 2022 image using a dust dy-

namical procedure. This procedure was developed by (Liu et al. 2016) and was modified for this work. In the simulations, the dust ejecta was assumed to be ejected from the sunlit side of comet E3 with a semi-opening angle of 90°. The starting time of the activity was assumed to be 2 March 2022, which is the epoch when comet E3 was first discovered, and the end time was the observation date. The size distribution of the dust grains followed a differential power-law distribution with an exponent of -3.5. The ejection velocity is related to the particle size and satisfies the relation $v_{\text{ej}} \sim 139\beta^{1/2}$ (Section 3.1). The escape velocity is approximately determined to be 1.47 m/s in the following section 4.2, and the upper limit size of the escape particles was preliminarily estimated to be 10 mm. Since the morphology of the dust coma on 10 October of 2022 is clearest in Figure 1, the simulation was conducted based on this image. The model simulations of the 10 October 2022 image for particle radii of 0.1 ~ 1 mm and 1 ~ 10 mm are showed in Figure 5. The nearly circular morphology in the image for 1 ~ 10 mm shows a distribution that is closely isotropic. The image for smaller particles (0.1 ~ 1 mm) shows a tadpole-like distribution, which is more closely aligned with the morphology of comet E3. The comparison between the observation and the model simulations of the 10 October 2022 image indicates that large particles lingering near the nucleus of comet E3 are sensitive to radiation pressure. The radii of the majority of these large particles range from 0.1 mm to 1 mm, and the upper limit of the particle size was therefore set to 1 mm.

4.2. Nucleus size and dust production rates

The effective scattering cross section C_e of the particles within the circular photometry aperture with a projected radius of 1000 km in Table 2 can be used to estimate the upper limit of the nucleus radius by $r_n = (C_e/\pi)^{1/2}$. To impose a stronger constraint on the radius of the nucleus, the aperture photometry of the nucleus was remeasured. A circular aperture with a fixed radius of

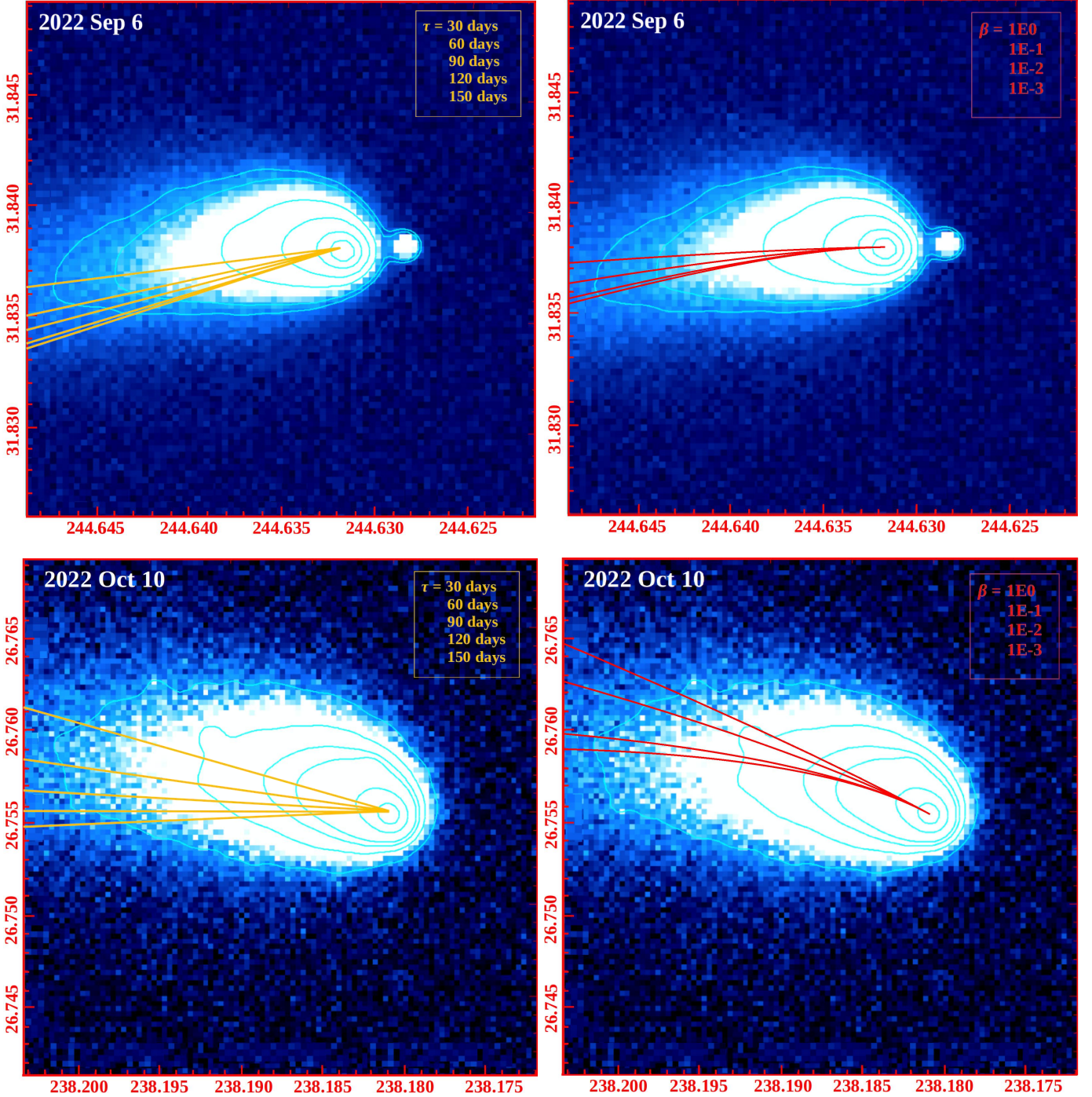


Fig. 4: Syndyne-synchrone grids overplotted on the observation images of comet E3. The yellow lines denote the synchrone of 30, 60, 90, 120, and 150 days (from top to bottom) before the respective observation dates, and the red lines denote the syndynes of $\beta = 1, 1 \times 10^{-1}, 1 \times 10^{-2},$ and 1×10^{-3} (from top to bottom). The images are oriented with north up (increasing DEC in degrees) and east to the left (increasing RA in degrees).

1000 km was still used to obtain the photometry of the nucleus. To reduce the dust contamination in the aperture on the nucleus photometry as much as possible, the background of the coma was determined in an annulus aperture with an inner radius of 1000 km and an outer radius of 2000 km. The minimum effective scattering cross sections of the nucleus were derived from the photometry of the image observed on 13 July 2022, giving $C_e = (24.45 \pm 0.02) \text{ km}^2$. Assuming that the nucleus of comet E3 is a homogeneous sphere and that the upper limit of size of

the nucleus is $r_n = (C_e/\pi)^{1/2} = (2.79 \pm 0.01) \text{ km}$, the upper limit of the mass of a spherical nucleus with an assumed bulk density of $\rho = 500 \text{ kg m}^{-3}$ (Groussin et al. 2019) is $(4.55 \pm 0.04) \times 10^{13} \text{ kg}$, and the upper limit of the escape velocity is 1.47 m s^{-1} .

The variation of C_e (Figure 6) can reflect the enhancement or weakening in the activity level of comet E3. The increase in the variable C_e implies that the inflow of the particles into the aperture exceeds the outflow, and the decrease implies that the outflow exceeds the inflow (Jewitt et al. 2020). From Kim et al.

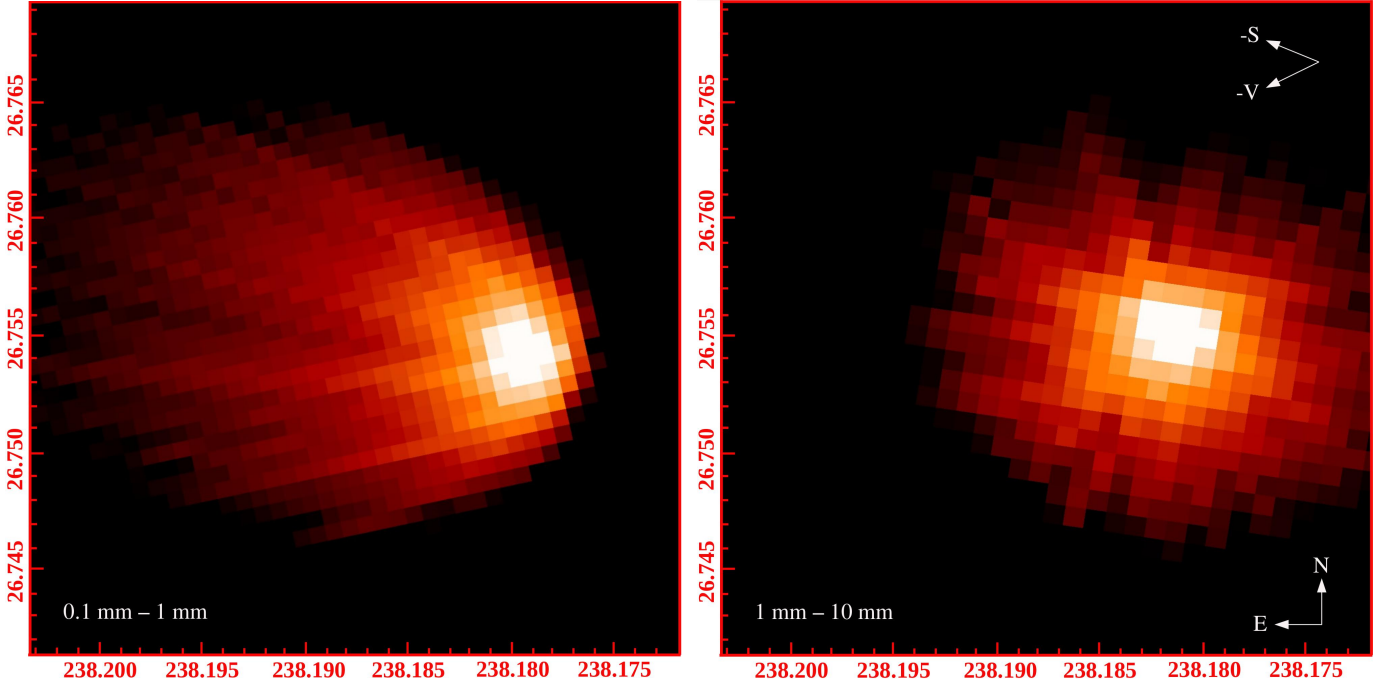


Fig. 5: Model simulations of the 10 October 2022 image. The ranges of the dust sizes used for the simulations are marked in the lower left corner of each panel. The projected Sun-E3 radial direction (-S) and the antivelocidity direction of the projected motion (-V) of comet E3 are indicated as white arrows. Each panel is oriented with north up (increasing DEC in degrees) and east to the left (increasing RA in degrees).

(2020), the average net dust production rate can be estimated by

$$\frac{dM}{dt} = \frac{4}{3} \frac{\rho \bar{a} C_e}{\tau_r}. \quad (4)$$

Here, $\bar{a} = a_{\max} \times a_{\min}$ is the mean radius of the dust grains, the value of which is estimated as $\bar{a} = 100 \mu\text{m}$ (see Section 4.1) under the assumption that the size distribution of the dust grains follows a differential power-law distribution with an exponent of -3.5. The bulk density of the particles is $\rho = 500 \text{ kg m}^{-3}$, as assumed earlier in this section. The values of C_e are seen in Table 2. The dwelling time of the particles within the aperture is estimated by $\tau_r = L/v_{\text{ej}}$, and an aperture with a radius of $L = 16000 \text{ km}$ was used for photometry. Considering that the ejection velocity of particles with an average radius of about $100 \mu\text{m}$ is about $v_{\text{ej}} \sim 14 \text{ m s}^{-1}$ according to Equation 1, the dwelling time is derived to be about $\tau_r \sim 1.1 \times 10^6 \text{ s}$. We substituted C_e within the aperture with a radius of 16000 km (Table 2) in Equation (4), and we derived the lower limit of the dust production rates as $\sim 241 \pm 3 \text{ kg s}^{-1}$ on 13 July 2022, $251 \pm 9 \text{ kg s}^{-1}$ on 26 July 2022, $281 \pm 6 \text{ kg s}^{-1}$ on 6 August 2022, $382 \pm 6 \text{ kg s}^{-1}$ on 6 September 2022, and $476 \pm 9 \text{ kg s}^{-1}$ on 10 October 2022. Assuming that the mean radius of the particles remains constant over time, it is found that the dust production rate increases with the decrease of the heliocentric distance (Table 1), suggesting that the activity is highly correlated with temperature.

4.3. Plane-crossing

The dust distribution perpendicular to the orbital plane of comet E3 can be determined from observation images taken on 06 July 2022 because at this time, the Earth was located almost in the orbital plane of comet E3 (Table 1). The tail width θ_{\perp} is shown

along the distance from the nucleus in Figure 7, where a broad tail is displayed, with $\theta_{\perp} < 28''$ up to $20''$ east of the nucleus and $\theta_{\perp} < 19''$ up to $10''$ west of the nucleus. The ejection speed perpendicular to the orbital plane v_{\perp} was derived from the tail width θ_{\perp} according to Jewitt et al. (2015)

$$v_{\perp} = \left[\frac{\beta g_{\odot}(1)}{8\ell R^2} \right]^{1/2} \theta_{\perp}, \quad (5)$$

where $g_{\odot}(1) = 0.006 \text{ m s}^{-2}$ is the solar gravitational acceleration at a heliocentric distance of 1 AU, and ℓ is the distance from the nucleus. The measured tail width was fit to Equation (5), as shown in Figure 7, and the result shows that the ejection speed is approximately $v_{\perp} \sim 89.8\beta^{1/2} \text{ m s}^{-1}$ on the east side of the nucleus. It is approximately $v_{\perp} \sim 83.1\beta^{1/2} \text{ m s}^{-1}$ on the west side of the nucleus. This $\beta^{1/2}$ dependence (i.e., $a^{-1/2}$ dependence) is basically consistent with that of the emission driven by gas (Kim et al. 2020). By substituting the estimated values of the mean grain radius of $a \sim 100 \mu\text{m}$ inferred from Section 4.1 into the aforementioned fitting formula, the ejection speed perpendicular to the orbital plane is obtained to be $v_{\perp} \sim 9 \text{ m s}^{-1}$. The result is approximately consistent with $v_{\text{ej}} \sim 14 \text{ m s}^{-1}$ for the grain radius of $a \sim 100 \mu\text{m}$ inferred from Section 3.1.

4.4. Sublimating area

Comet E3 is continuously active, and its activity level increases as the heliocentric distance decreases, suggesting that the sublimation of ice is likely the origin of the activity. Following Hui et al. (2019), the mass flux of the sublimation of ice, denoted $f_s(T)$, can be calculated using the energy balance equation,

$$\frac{S_{\odot}}{R^2}(1 - A) = \chi \left[\epsilon \sigma T (R)^4 + H_s f_s(T) \right], \quad (6)$$

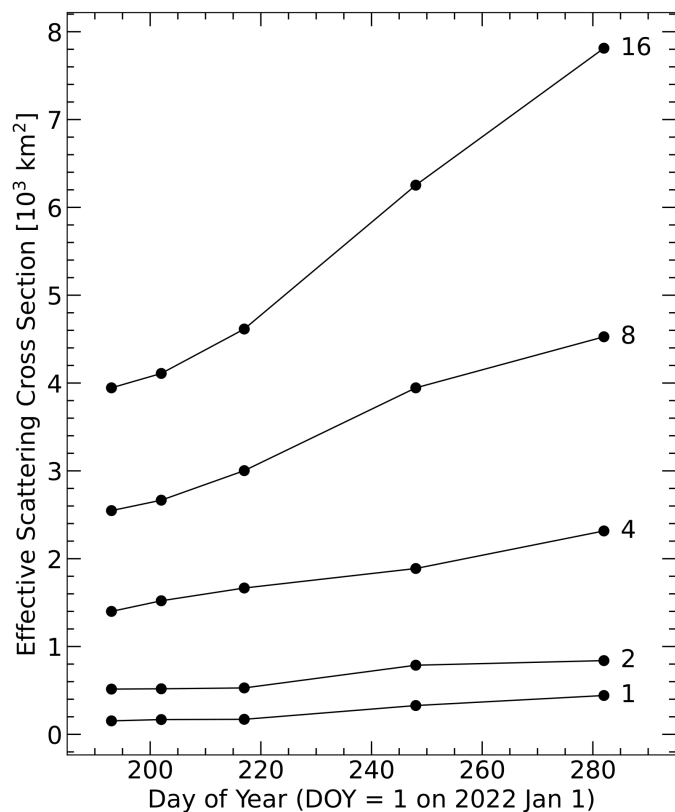


Fig. 6: Effective scattering cross section vs. epoch of observation (day of year = 1 on 1 January 2022) for each of the five apertures with different radii. The radius of each aperture is given at the right side of each line (in units of 10^3 km). The error bars are smaller than the size of the data points, causing them to be hidden behind the points.

where $S_{\odot} = 1361 \text{ W m}^{-2}$ is the solar constant, $\sigma = 5.67 \times 10^{-8} \text{ W m}^{-2} \text{ K}^{-4}$ is the standard value of the Stefan–Boltzmann constant, $A = 0.04$ is the assumed bond albedo, and $H_s(T)$ is the latent heat of volatile substances at a specific temperature, T . The distribution coefficients of the incident heat and the effective emissivity are assumed to be $\chi = 2$ and $\epsilon = 0.9$, respectively. The equilibrium temperature of comet E3 varies in the range of about $162 \text{ K} < T < 202 \text{ K}$ when the heliocentric distance is between 1.83 AU and 2.86 AU. Estimated from the Equation (6), the mass flux of the H_2O sublimation varies approximately in the range of $1.68 \times 10^{-5} \text{ kg m}^{-2} \text{ s}^{-1}$ (2.86 AU) $< f_s < 4.47 \times 10^{-5} \text{ kg m}^{-2} \text{ s}^{-1}$ (1.83 AU).

The OH number production rate Q_{OH} of comet E3 is approximately $(1.16 \pm 0.23) \times 10^{28} \text{ s}^{-1}$ in October 2022 (Jehin et al. 2022a), from which the number production rate of water for comet E3 is estimated as $Q_{\text{H}_2\text{O}} = (1.23 \pm 0.24) \times 10^{28} \text{ s}^{-1}$. As a result, the mass production rate of water is derived to be $\dot{M}_{\text{water}} \sim (368 \pm 72) \text{ kg s}^{-1}$ in October 2022. Assuming that the nucleus of comet E3 is a homogeneous sphere, the lower limit of the size of this nucleus that can maintain the observed sublimation activity is estimated according to (Jewitt & Luu 2019)

$$r_n \gtrsim \sqrt{\frac{\dot{M}_{\text{water}}}{4\pi f_s}}. \quad (7)$$

By substituting the estimated values of \dot{M}_{water} and f_s (for H_2O) into Equation (7), the lower limit of the size of the nucleus is

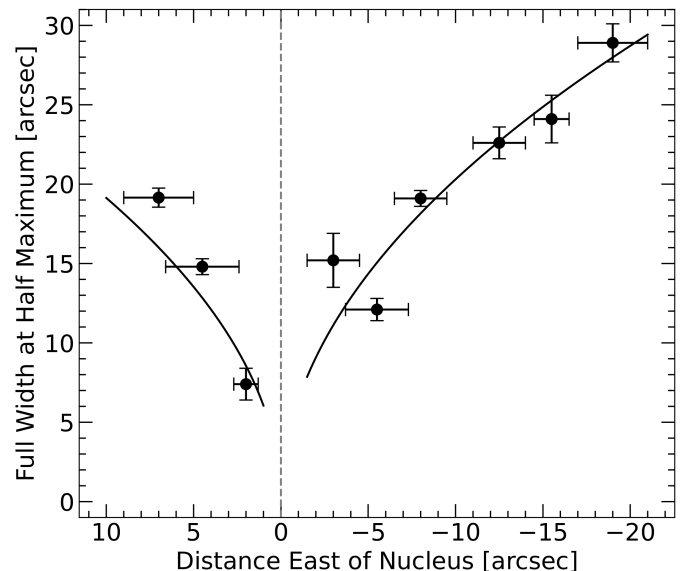


Fig. 7: FWHM of the dust tail of comet E3 vs. distance from the nucleus in the observation image taken on 10 October 2022 when Earth was located almost in the orbital plane of comet E3. The horizontal error bars show the distance range along the tail that was used to measure the FWHM, and the vertical bars indicate the range of uncertainties of the FWHM profiles. The red and blue lines denote the best-fitting relation $\theta_{\perp} \propto l^{1/2}$ between the FWHM of the tail and the distance from the nucleus.

determined to be $\sim (0.81 \pm 0.07) \text{ km}$, which corresponds to a sublimating area of about $8.2 \times 10^6 \text{ m}^2$. In comparison, 2I/2019 Q4 (Borisov), which is classified as an interstellar comet, was activated before reaching its perihelion due to the sublimation of volatile substances, and (Jewitt & Luu 2019) analyzed the data of 2I obtained with a similar observation geometry and estimated its sublimating area to be approximately $1.5 \times 10^6 \text{ m}^2$.

4.5. Particular characteristics of E3 compared with other comets

In this section, we present a comparative analysis of the characteristics of comet E3 with those of comets belonging to different types. Figure 8a illustrates the brightness profiles of different types of comets, including 11 short-period comets, 14 long-period comets, and comet E3. Figure 8a clearly shows that the brightness indices of the majority of the long-period comets are higher than -1.5 , whereas the brightness indices of the short-period comets are more widely distributed, and their heliocentric distances during outbursts are smaller than 7 AU. Notably, when the range of the heliocentric distance is narrowed to about [1.7, 3.4] AU (i.e., where the observations of comet E3 that were used for analysis in this study were taken (see Table 1)), it becomes evident that the indices of the short-period comets are close to those of the brightness profiles of comet E3.

Figure 8b depicts the dust mass production rates for eight short-period comets, six long-period comets, and comet E3, the data of which are from a different literature collection from the brightness profiles shown in Figure 8a. When we compare the dust production rates of comets within the heliocentric distance range of about [1.7, 3.4] AU, it becomes evident that the activity level of comet E3 is significantly lower than those of other long-period comets. Furthermore, the values of the dust production

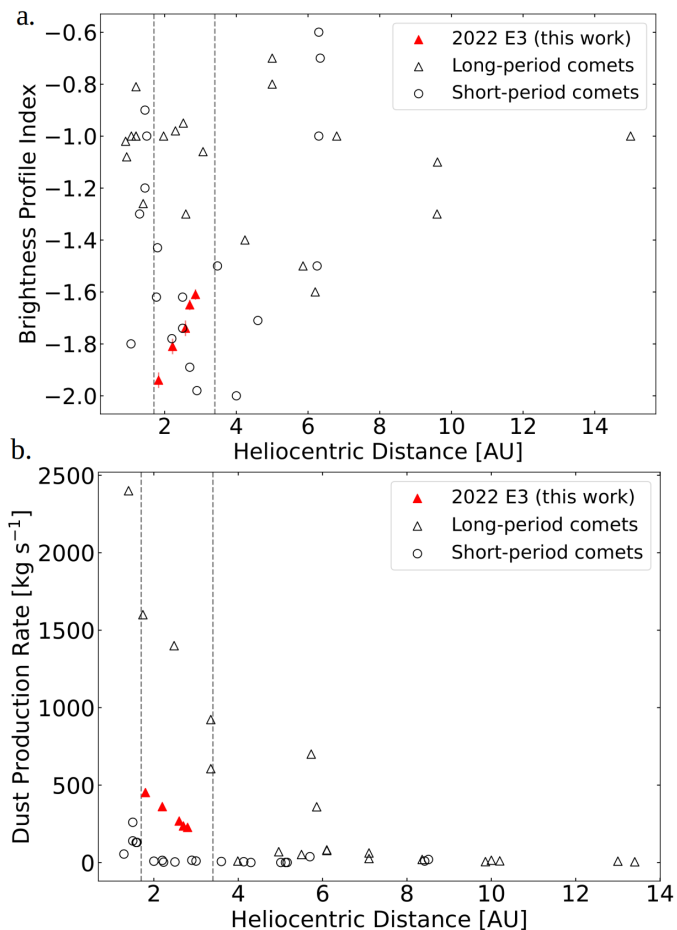


Fig. 8: Comparison of the activity characteristics of comet E3 (see Section 3.1 and Section 4.2) with those of comets belonging to different types (see Appendix A). a) Brightness index vs. heliocentric distance of comet E3, long-period comets, and short-period comets. b) Dust production rates vs. the heliocentric distance of comet E3, long-period comets, and short-period comets. The error bars of the E3 production rates are obscured by the data points. The two vertical dashed lines represent the heliocentric distances of 1.7 AU and 3.4 AU, respectively, within the range of which the observations of comet E3 that were used for analysis in this study were taken (see Table 1). It should be noted that the data of the listed brightness profiles and dust production rates are from two different literature collections.

rates of comet E3 at different heliocentric distances are closer to those of the short-period comets. Thus, when we correlate the activity level of comets with their heliocentric distances, as indicated in Figure 8a and 8b, and without considering other factors that might influence the activity level, such as the nucleus size, comet E3 exhibits a duality. In other words, while the orbital characteristics of E3 classify it as a long-period comet, its activity profile is more closely aligned with those of short-period comets within the heliocentric distance range where the observation images of comet E3 that were used for the analysis in this study were taken.

5. Summary

This paper analyzed the activity of the long-period comet 2022 E3 (ZTF) at five epochs between 13 July 2022 and 10 October 2022. The results are listed below.

1. We showed that the brightness distribution indices of the inner coma are lower than -1.5, suggesting that the particles from comet E3 are released continuously and the process of dust emission is in nonsteady state. The increase in the dust production rate with the decreasing heliocentric distance might be one reason for the nonsteady-state nature of the dust emission process.
2. The syndyne fitting results show that dust particles larger than about 10 μm contribute significantly to the observed tail. The model simulations of the 10 October 2022 image show that the radii of the majority of the large particles lingering near the nucleus range from 0.1 mm to 1 mm.
3. The radius range of the nucleus of comet E3 is estimated as between 0.81 ± 0.07 km and 2.79 ± 0.01 km, with an assumed albedo of 0.1. The dust production rates increased continuously from 241 ± 3 kg s⁻¹ in July 2022 to 476 ± 9 kg s⁻¹ in October 2022.
4. The dependence of the ejection velocity on the grain size is basically consistent with that of emission driven by gas. The ejection speed perpendicular to the orbital plane of the particle with an average radius of 100 μm is estimated as ~ 9 m s⁻¹.
5. The estimated water production rate is $\sim 368 \pm 72$ kg s⁻¹. The lower limit of the equilibrium sublimating area that can maintain the observed sublimation activity is approximately 8.2×10^6 m², which corresponds to a sphere with a radius of 0.81 ± 0.07 km.
6. Within the heliocentric distance range of about [1.7, 3.4] AU where the observation images of comet E3 that were used for the analysis in this study were taken, the following phenomena are found. The brightness indices of comet E3 are close to those of short-period comets. In addition, the values of the dust production rates of comet E3 are lower than those of long-period comets, but they agree well with those of short-period comets.

Acknowledgements. This work was supported by the National Natural Science Foundation of China (No. 12002397, 12311530055 and 62388101), and the Shenzhen Science and Technology Program (Grant No. ZDSYS20210623091808026). We thank Shangfei Liu for helpful discussions and suggestions. The data used in this work is generated as detailed in the text and will be shared on reasonable request to the corresponding author.

References

- Bellm, E. C., Kulkarni, S. R., Graham, M. J., et al. 2018, Publications of the Astronomical Society of the Pacific, 131, 018002
- Bertin, E. & Arnouts, S. 1996, Astronomy and astrophysics supplement series, 117, 393
- Betzler, A. & de Sousa, O. 2023, Astronomische Nachrichten, e20220084
- Bodewits, D., Farnham, T., A'Hearn, M., et al. 2014, The Astrophysical Journal, 786, 48
- Bolin, B., Masci, F., Duev, D., et al. 2024, Monthly Notices of the Royal Astronomical Society: Letters, 527, L42
- Bolin, B. T., Fernandez, Y. R., Lisse, C. M., et al. 2021, The Astronomical Journal, 161, 116
- Bolin, B. T., Masci, F. J., Ip, W.-H., et al. 2022, Minor Planet Electronic Circulars, 2022-F13
- Borsovsky, J., Nauta, K., Jiang, J., et al. 2021, Proceedings of the National Academy of Sciences, 118, e2113315118
- Burns, J. A., Lamy, P. L., & Soter, S. 1979, Icarus, 40, 1
- Clements, T. D. & Fernandez, Y. 2021, The Astronomical Journal, 161, 73

- de Val-Borro, M., Bockelée-Morvan, D., Jehin, E., et al. 2014, *Astronomy & Astrophysics*, 564, A124
- Delahodde, C., Meech, K., Hainaut, O., & Dotto, E. 2001, *Astronomy & Astrophysics*, 376, 672
- Epifani, E. M., Snodgrass, C., Perna, D., et al. 2016, *Planetary and Space Science*, 132, 23
- Farnham, T. L. 2009, *Planetary and Space Science*, 57, 1192
- Farnham, T. L. & Cochran, A. L. 2002, *Icarus*, 160, 398
- Farnham, T. L. & Schleicher, D. G. 2005, *Icarus*, 173, 533
- Finson, M. & Probst, R. F. 1968, *The Astrophysical Journal*, 154, 327
- Forbes, J. C. & Loeb, A. 2019, *The Astrophysical Journal Letters*, 875, L23
- Garcia, R. S. & Gil-Hutton, R. 2021, *Planetary and Space Science*, 206, 105308
- Groussin, O., Attree, N., Brouet, Y., et al. 2019, *Space Science Reviews*, 215, 1
- Guilbert-Lepoutre, A., Schulz, R., Rožek, A., et al. 2014, *Astronomy & Astrophysics*, 567, L2
- Hands, T. & Dehnen, W. 2020, *Monthly Notices of the Royal Astronomical Society: Letters*, 493, L59
- Hui, M.-T., Farnocchia, D., & Micheli, M. 2019, *The Astronomical Journal*, 157, 162
- IRSA. 2020, IRSA Simple Image Access (SIA) v2 Service
- Ishiguro, M., Watanabe, J.-i., Sarugaku, Y., et al. 2010, *The Astrophysical Journal*, 714, 1324
- Ivanova, O., Rosenbush, V., Luk'yanyk, I., et al. 2021, *Astronomy & Astrophysics*, 651, A29
- Ivanova, O., Rosenbush, V., Luk'yanyk, I., et al. 2023, *Astronomy and Astrophysics*, 672, A76
- Ivanova, O. V., Dlugach, J. M., Afanasiev, V. L., Reshetnyk, V. M., & Korsun, P. P. 2015, *Planetary and Space Science*, 118, 199
- Jayakrishnan, R., Dev L, R., & Aalim, M. 2023, *Research Notes of the AAS*, 7, 44
- Jehin, E., Donck, M. V., Manfroid, J., & Moulane, Y. 2022a, *The Astronomer's Telegram*, 15743, 1
- Jehin, E., Gillon, M., Queloz, D., et al. 2011, *The Messenger*, 145
- Jehin, E., Vander Donck, M., Manfroid, J., et al. 2022b, *The Astronomer's Telegram*, 15822, 1
- Jewitt, D., Agarwal, J., Hui, M.-T., et al. 2019a, *The Astronomical Journal*, 157, 65
- Jewitt, D., Agarwal, J., Weaver, H., Mutchler, M., & Larson, S. 2015, *The Astrophysical Journal*, 798, 109
- Jewitt, D., Kim, Y., Luu, J., & Graykowski, A. 2019b, *The Astronomical Journal*, 157, 103
- Jewitt, D., Kim, Y., Mutchler, M., et al. 2020, *The Astrophysical Journal Letters*, 896, L39
- Jewitt, D. & Luu, J. 2019, *The Astrophysical Journal Letters*, 886, L29
- Jewitt, D. & Meech, K. J. 1987, *Astrophysical Journal*, Part 1 (ISSN 0004-637X), vol. 317, June 15, 1987, p. 992-1001. NASA-supported research., 317, 992
- Jones, G. & Snodgrass, C. 2019, in *Geophysical Research Abstracts*, Vol. 21
- Joye, W. A. & Mandel, E. 2003, in *Astronomical data analysis software and systems XII*, Vol. 295, 489
- Kareta, T. R. 2021, PhD thesis, The University of Arizona
- Kim, Y., Jewitt, D., Agarwal, J., et al. 2022, *The Astrophysical Journal Letters*, 933, L15
- Kim, Y., Jewitt, D., Mutchler, M., et al. 2020, *The Astrophysical Journal Letters*, 895, L34
- Knight, M., Holt, C., Villa, K., Skiff, B., & Schleicher, D. 2023, *The Astronomer's Telegram*, 15879, 1
- Korsun, P. P., Rousselot, P., Kulyk, I. V., Afanasiev, V. L., & Ivanova, O. V. 2014, *Icarus*, 232, 88
- Kueppers, M. 2023, The Comet Interceptor probe could visit a stunning object like the green C/2022 E3 (ZTF), accessed on Date
- Kulyk, I., Korsun, P., Lukyanyk, I., et al. 2021, *Icarus*, 355, 114156
- Lamy, P., Toth, I., Jorda, L., et al. 2002, *Icarus*, 156, 442
- Lamy, P., Toth, I., Jorda, L., Weaver, H., & A'Hearn, M. 1998, *Astronomy and Astrophysics*, v. 335, p. L25-L29 (1998), 335, L25
- Lejoly, C., Harris, W., Samarasinha, N., et al. 2022, *The Planetary Science Journal*, 3, 17
- Li, J. & Jewitt, D. 2015, *The Astronomical Journal*, 149, 133
- Lippi, M., Vander Donck, M., Faggi, S., et al. 2023, *Astronomy & Astrophysics*, 676, A105
- Liu, X., Sachse, M., Spahn, F., & Schmidt, J. 2016, *Journal of Geophysical Research: Planets*, 121, 1141
- Lowry, S., Fitzsimmons, A., Lamy, P., & Weissman, P. 2008, *The Solar System Beyond Neptune*, 397
- Manzini, F., Oldani, V., Ochner, P., Bedin, L. R., & Reguitti, A. 2023, *The Astronomer's Telegram*, 15909, 1
- Meech, K., Bauer, J., & Hainaut, O. 1997, *Astronomy and Astrophysics*, v. 326, p. 1268-1276, 326, 1268
- Moore, K., Courville, S., Ferguson, S., et al. 2021, *Planetary and Space Science*, 197, 105137
- Moreno, F., Muñoz, O., Gutiérrez, P. J., et al. 2017, *Monthly Notices of the Royal Astronomical Society*, 469, S186
- Moreno, F., Pozuelos, F., Aceituno, F., et al. 2012, *The Astrophysical Journal*, 752, 136
- Moreno, F., Snodgrass, C., Hainaut, O., et al. 2016, *Astronomy & Astrophysics*, 587, A155
- Mugrauer, M. 2023, *The Astronomer's Telegram*, 15876, 1
- Mumma, M. J. & Charnley, S. B. 2011, *Annual Review of Astronomy and Astrophysics*, 49, 471
- Nesvorný, D. 2018, *Annual Review of Astronomy and Astrophysics*, 56, 137
- Nicolini, M., Cavicchio, F., & Facchini, M. 2003, *Astroart 5.0*, MSB Software
- Opitom, C., Jehin, E., Manfroid, J., et al. 2015, *Astronomy & Astrophysics*, 584, A121
- Reyniers, M., Degroote, P., Bodewits, D., Cuypers, J., & Waelkens, C. 2009, *Astronomy & Astrophysics*, 494, 379
- Rousselot, P., Korsun, P., Kulyk, I., et al. 2014, *Astronomy & Astrophysics*, 571, A73
- Rousselot, P., Korsun, P., Kulyk, I., Guilbert-Lepoutre, A., & Petit, J.-M. 2016, *Monthly Notices of the Royal Astronomical Society*, 462, S432
- Rousselot, P., Kryszyńska, A., Bartczak, P., et al. 2021, *Monthly Notices of the Royal Astronomical Society*, 507, 3444
- Schulz, R. & Stüwe, J. A. 2002, *Earth, Moon, and Planets*, 90, 195
- Schwamb, M. E., Knight, M. M., Jones, G. H., et al. 2020, arXiv preprint arXiv:2002.01744
- Shi, J., Ma, Y., & Zheng, J. 2014, *Monthly Notices of the Royal Astronomical Society*, 441, 739
- Shi, J., Xu, R., Ma, Y., et al. 2023, *The Astrophysical Journal*, 943, 26
- Snodgrass, C. & Jones, G. H. 2019, *Nature communications*, 10, 5418
- Soja, R., Sommer, M., Herzog, J., et al. 2015, *Astronomy & Astrophysics*, 583, A18
- Tricarico, P., Samarasinha, N. H., Sykes, M. V., et al. 2014, *The Astrophysical Journal Letters*, 787, L35
- Wiegert, P. & Tremaine, S. 1999, *Icarus*, 137, 84
- Woodward, C. E., Wooden, D. H., Harker, D. E., et al. 2021, *The Planetary Science Journal*, 2, 25
- Xu, R., Shi, J., Ma, Y., Li, F., & Yuan, Y. 2022, *Astronomy and Astrophysics*, 665, A79
- Yang, B., Jehin, E., Pozuelos, F. J., et al. 2019, *Astronomy & Astrophysics*, 631, A168

Appendix A: Information about the comets in Figure 8

Table A.1: Activity characteristics of the comets

Name	Type ^a	q^b (R^c)	\dot{M}^d (R^c)	References
17P	S	-	2.8 (2.2), 5.4 (4.1), 0.6 (5.0), 0.8 (5.1), 0.6 (5.1),	[1]
19P	S	-1.2 (1.6), -1.3 (1.4)	-	[2]
22P	S	-	130.0 (1.6), 260.0 (1.6)	[3], [4]
29P	S	-	38.0 (5.8)	[5]
45P	S	-1.8 (0.5)	-	[6]
46P	S	-1.1 (1.1), -1.6 (2.5), -1.4 (1.8)	4.0 (2.5)	[6], [7], [8]
60P	S	-1.6 (1.7)	-	[9]
64P	S	-0.9 (1.6)	-	[10]
66P	S	-	55.0 (1.3)	[11]
67P	S	-2.0 (2.9), -1.9 (2.7)	15.0 (2.9), 0.5 (4.3)	[12], [13], [14]
67P	S	-1.7 (2.5), -1.8 (2.2)	10.0 (3.0), 7 (3.6)	[12], [13], [14]
81P	S	-1.0 (1.7), -1.3 (1.7)	-	[15]
174P	S	-1.0 (6.3)	20.0 (8.5), 10 (8.4)	[16], [17]
228P	S	-1.5 (3.5)	-	[18]
2019 LD ₂	S	-1.7 (4.6)	-	[19]
C/1996 Q1	L	-1.0 (1.2)	-	[20]
C/1999 S4	L	-1.0 (0.9)	-	[21]
C/2002 VQ94	L	-	20.0 (8.4), 6.0 (9.9), 5.0 (13.4)	[22]
C/2004 Q2	L	-0.8 (1.2), -1.0 (1.2)	-	[23]
C/2006 S3	L	-1.5 (5.9)	360.0 (5.9), 82.0 (6.1), 9.0 (13.9), 52.0 (5.6), 11.0 (10.3)	[17], [24]
C/2006 S3	L	-	15.0 (10.0), 26.0 (7.2), 78.0 (6.1), 62.0 (7.2)	[9], [24]
C/2006 OF2	L	-1.4 (4.2)	-	[25]
C/2006 W3	L	-	70.0 (5.0), 676.0 (3.3), 923 (3.3), 606 (3.3)	[26]
C/2009 P1	L	-1.0 (2.0)	700.0 (5.7), 1400.0 (2.5)	[27], [28]
C/2010 X1	L	-1.6 (2.9)	-	[29]
C/2010 S1	L	-0.7 (5.0), -1.6 (6.2)	-	[30]
C/2011 KP36	L	-0.8 (5.0)	-	[31]
C/2012 F6	L	-1.3 (1.9)	-	[32]
C/2014 B1	L	-1.1 (9.6), -1.3 (9.6)	-	[33], [34]
C/2014 S2	L	-1.0 (2.3)	-	[35]
C/2013 A1	L	-	10.0 (3.8)	[36]
C/2013 US10	L	-	1600.0 (1.7), 2400.0 (1.4)	[37]
C/2017 K2	L	-1.0 (15.9), -1.0 (13.8)	-	[38]

^a S: short-period comet; L: long-period comet. ^b Brightness index rounded to one decimal place. ^c Heliocentric distance rounded to one decimal place, in AU. ^d Dust production rate rounded to one decimal place, in kg/s.

References: [1] Ishiguro et al. (2010); [2] Farnham & Cochran (2002); [3] Lamy et al. (2002); [4] Moreno et al. (2012); [5] Clements & Fernandez (2021); [6] Lejoly et al. (2022); [7] Meech et al. (1997); [8] Lamy et al. (1998); [9] Shi et al. (2023); [10] Xu et al. (2022); [11] Yang et al. (2019); [12] Moreno et al. (2016); [13] Soja et al. (2015); [14] Guilbert-Lepoutre et al. (2014); [15] Farnham & Schleicher (2005); [16] Rousselot et al. (2021); [17] Rousselot et al. (2016); [18] Shi et al. (2014); [19] Bolin et al. (2021); [20] Guilbert-Lepoutre et al. (2014); [21] Schulz & Stüwe (2002); [22] Korsun et al. (2014); [23] Reyniers et al. (2009); [24] Rousselot et al. (2014); [25] Kulyk et al. (2021); [26] de Val-Borro et al. (2014); [27] Epifani et al. (2016); [28] Bodewits et al. (2014); [29] Li & Jewitt (2015); [30] Ivanova et al. (2015); [31] Ivanova et al. (2021); [32] Opitom et al. (2015); [33] Jewitt et al. (2019b); [34] Ivanova et al. (2023); [35] Betzler & de Sousa (2023); [36] Tricarico et al. (2014); [37] Woodward et al. (2021); [38] Jewitt et al. (2019a).